



OPEN

The October 23, 2011, Van (Turkey) earthquake and its relationship with neighbouring structures

SUBJECT AREAS:

TECTONICS
GEOLOGY
SEISMOLOGY
GEODYNAMICSReceived
4 June 2013Accepted
10 January 2014Published
12 March 2014

Correspondence and requests for materials should be addressed to M.M. (marco.moro@ingv.it)

Moro M.¹, Cannelli V.¹, Chini M.², Bignami C.¹, Melini D.¹, Stramondo S.¹, Saroli M.^{1,3}, Picchiani M.¹, Kyriakopoulos C.⁴ & Brunori C. A.¹

¹Istituto Nazionale di Geofisica e Vulcanologia, via di Vigna Murata 605, 00143 Rome, Italy, ²Centre de Recherche Public - Gabriel Lippmann, 41, rue du Brill, L-4422 Belvaux, Luxembourg, ³Università degli Studi di Cassino e del Lazio Meridionale, DICeM-Dipartimento di Ingegneria Civile e Meccanica, Cassino, Italy, ⁴School of Earth and Atmospheric Sciences, Georgia Institute of Technology, Atlanta, Georgia (USA).

The present work reports the analysis of a possible relationship due to stress transfer between the two earthquakes that hit the province of Van, Eastern Turkey, on October 23, 2011 ($M_w = 7.2$) and on November 9, 2011 ($M_w = 5.6$). The surface displacement field of the mainshock has been obtained through a combined data set made up of differential interferograms from COSMO-SkyMed and ENVISAT satellites, integrated with continuous GPS recordings from the Turkish TUSAGA-AKTIF network. This allowed us to retrieve the geometry and the slip distribution of the seismic source and to compute the Coulomb Failure Function (CFF) variation on the aftershock plane, in order to assess a possible causal relationship between the two events. Our results show that the November 9 earthquake could have been triggered by the October 23 shock, with transferred stress values largely exceeding 1 bar.

The occurrence of a seismic event perturbs the stress field within the Earth crust, altering the probability of occurrence of a second strong event along nearby faults. This phenomenon is known as *fault interaction*, and the physical mechanism at its basis is known as the Coulomb Stress Triggering¹. In literature it has been shown that even weak increments of stress can trigger large seismic events², if the relative seismogenic structures are close to the end of their seismic cycle; furthermore, the interaction between two seismic events may occur both within long interseismic periods³ and smaller time intervals^{4–6}. Stress field perturbations cannot be instrumentally detected, but can be numerically simulated by means of mathematical models^{2,7–9}. Several studies demonstrate that the distribution of aftershocks and the variations of the seismicity rates are generally explained in terms of the Coulomb failure criterion^{1,2,10–12}, which allows to interpret a shear stress exceeding a certain fraction of the normal stress as an increased probability of failure¹⁰. Several physical-static prediction models based on the Coulomb criterion have been proposed^{13,14}; these models have been widely applied for the redefinition of the regional seismic hazard following earthquakes^{12,15–18}.

The province of Van (Eastern Turkey) has been struck by two strong earthquakes in a few days. The first earthquake occurred on October 23, 2011 ($M_w = 7.2$), 30 km N of Van city, while the second took place on November 9, 2011 ($M_w = 5.6$) few kilometers to the South¹⁹ (Fig. 1a), in the Edremit subprovince. A significant aftershock activity was recorded after the first shock over the Van region (Fig. 1a). The $M_w 7.2$ Van earthquake occurred along a ENE-WSW fault, previously recognized by Kein²⁰, who attributes to it a main right lateral strike slip mechanism. However the CMT (Centroid Moment Tensor) solution from USGS and GFZ indicates a pure reverse fault mechanism (Fig. 1a)^{21,22}, while the Harvard CMT solution is a mixed reverse-right lateral mechanism. Concerning the November 9 (hereafter Edremit-Van) earthquake, the Kandilli Observatory and Earthquake Research Institute (KOERI) CMT solution indicates a dominant strike slip mechanism²³.

Turkey is surrounded by three main plates, the African, Eurasian and Arabian ones, characterized by relevant tectonic activity. Other two minor plates are also present in this region, the Aegean and the Anatolian ones. The relative motion amongst the above mentioned plates has generated some of the major tectonic features of Turkey: the Aegean Arc, the West Anatolian Graben Complexes, the North Anatolian Fault Zone, the East Anatolian Fault Zone, the North East Anatolian Fault Zone, the Bitlis Thrust Zone, and the Caucasus (Fig. 1b)²⁴. The study area is located where the Arabian Plate, that moves towards north-northeast, collides with the Eurasia along the Bitlis Thrust Zone, a complex collisional boundary located north of the fold-and-thrust belt of the Arabian



platform. This suture zone corresponds with the Van Lake region from which the other smaller plates move symmetrically away, forced by the Arabian plate movement (see Fig. 1b)²⁵. In this sector the GPS velocities indicate a NW-oriented motion of 18 ± 2 mm/year relative to the Eurasia²⁶, causing an intense seismic activity. This latter is associated with ENE-WSW and NW-SE conjugate strike-slip faults, of dextral and sinistral character, parallel to the North and the East Anatolian fault zones. Among the major structures in the area the Çaldıran Fault, Erciş Fault, İğdır Fault, Malazgirt Fault, Süphan Fault, Kağızman Fault Zone, Tutak Fault Zone and Northeast Anatolian Fault Zone can also be mentioned. These structures are compatible with NNE-SSW compression and WNW-ESE extension in the region that well-matched the reverse mechanism related to the Van earthquake.

Several large earthquakes have struck this region both in historical and instrumental ages. The most relevant known that damaged the city of Van was the 1648 event (March 31, $M_w \approx 6.6$), which has been associated with the E-W trending Gurpinar thrust, located south of Van²⁷. The 1715 event (March 8, $M_w \approx 6.6$) was located between the eastern termination of Derik fault and Van²⁸, whilst the 1903 (April 28, $M_w \approx 7$) Malazgirt earthquake occurred on a NNE-SSW trending structure²⁹. One of the most recent and destructive event was the November 24, 1976 ($M_s = 7.3$), Caldıran earthquake, causing more than 4,000 casualties and intense damaging in a 2,000 km² area³⁰. The responsible fault was a N 110° – 135° , 50 km long, right lateral strike-slip mechanism, with observed horizontal displacements varying between 2.5 and 3.5 m and a vertical displacement of about 50 cm.

We have applied Differential Interferometric SAR (DInSAR) technique to investigate the surface displacement due to the 2011 $M_w 7.2$ and $M_w 5.6$ shocks. Different datasets have been used. In order to study the mainshock, a pair of COSMO-SkyMed Stripmap data has been processed, together with two ENVISAT SAR images. An additional dataset composed of two TerraSAR-X pairs was available to measure the surface effects induced by the second event and to infer its fault geometry. Finally, in order to remove the topographic phase contribution, we used the Shuttle Radar Topographic Mission (SRTM) digital elevation model. To better constrain the deformation field, we integrated in our analysis the DInSAR dataset with coseismic displacement field from 20 GPS stations belonging to the Turkish CGPS network, whose static offsets were assembled by Dr. Rahsan Cakmak (TUBITAK MRC EMSI) and are available at <http://supersites.earthobservations.org/van.php>.

Results

DInSAR processing has been applied to a SAR dataset composed of three pairs of Very High Resolution (VHR) X-band images (in strip-map mode^{31,32}), one acquired from COSMO-SkyMed (10/10/2011–23/10/2011), i.e. related to the main event, and the other two from TerraSAR-X (9/11/2011–20/11/2011 and 31/10/2011–11/11/2011) satellites. The frame available from COSMO-SkyMed partially covers the epicentral region, with the epicenter of October 23 mainshock located few km out of the area of measurement (Fig. 2). The measured surface movements have a maximum deformation along the LOS (Line Of Sight) of about 1.0 m in the uplifting sector, while in the southern portion of the interferogram a subsidence up to 0.02 m has been detected. As the COSMO-SkyMed images did not cover the northern section of the deformed area, a pair of SAR images acquired by ENVISAT platform (22/07/2011–19/11/2011) has been used in order to better assess the induced surface displacement in the upper region of the displacement field, (Fig. 2). Despite the ENVISAT data pair covers a time interval including the November 9 event, the northern portion of the displacement field can be considered free of the effects of the second earthquake because of the large epicentral distance. Two TerraSAR-X interferograms, along descending and ascending orbits (Supplementary material Fig. S1), have been

used to investigate the effects of the November 9 earthquake. These interferograms clearly highlighted that the November 9 event did not contribute to the deformation induced by the main shock on October 23.

TerraSAR-X interferograms show different fringe patterns, probably due to the strike slip mechanism, that implies most of the movement along an horizontal axis. Unfortunately TerraSAR-X data do not allow to solve the ambiguity of the E-W and N-S conjugate planes, either because the coseismic displacement field is partially detected, or due to the moderate magnitude of the buried fault. Nevertheless, the E-W plane solution can be considered the most probable as suggested by Akinci et al.³³ and supported by field evidence³⁴.

We retrieved the source model for the Van earthquake from a two-step joint inversion of DInSAR and GPS data. In a first step, the geometry and extension of the source have been determined assuming uniform slip on the fault plane. The probability distributions of the fault plane parameters (Fig. S2) have been obtained by evaluating the Bayesian integrals with a numerical Markov-Chain Monte Carlo integration scheme³⁵. The most probable model (Table 1) has a strike of 252 degrees and dips NNW at 50 degrees. The strike value is consistent with the orientation of the CMT focal plane and with geodetic models^{36,37}. The modeled dip angle is slightly larger than the value from Harvard CMT, but is consistent with geodetic indications of a steeply dipping fault in the range 40–55 degrees³⁷. The geodetic magnitude for the uniform-slip model is $M = 7.08$ if a shear crustal modulus of 30 GPa is assumed.

After the definition of the fault geometry, a linear inversion has been performed in order to estimate the slip distribution on the rupture plane. In this step, the size of the fault plane has been extended in order to better account for slip heterogeneities. The resulting slip distribution is shown in Figure 3 and has a cumulative geodetic magnitude of $M = 7.12$, in good agreement with the seismological estimates. The resulting pattern shows a deep high-slip patch, with peak slip (3.8 m) located at 15 km depth, with the epicentral location (provided by KOERI) located at its lower boundary; the location and extents of the bulk slip area is consistent with results by Fielding et al.³⁶. This geometry suggests that the rupture nucleated in the deep central portion of the fault and migrated towards the surface. The direction of slip vectors show dominant reverse-left mechanism; a patch with moderate reverse-right slip values at the southeastern tip of the modeled fault is probably an artifact, because this edge of the fault is beneath water and therefore is not constrained by SAR data. The modeled deformation field (Figures 4a and 4b) reproduces correctly the observed displacement; residuals of a few centimeters found on the eastern portion of the fault plane surface trace may be ascribed to a change in the strike direction³⁷, and/or to the activation of secondary shallow ruptures³⁸.

Once defined the source model for the Van earthquake, the role of this event in promoting the rupture of the Van-Edremit earthquake through a Coulomb Failure Function (CFF) analysis can be assessed. The CFF is evaluated by computing the incremental stress tensor produced by the elastic dislocation of the Van earthquake, projecting it on the rupture plane of the Van-Edremit earthquake and evaluating the relative contributions of the normal and shear stresses. Positive or negative variations of the CFF indicate that the perturbation to stress field is acting to promote or oppose the rupture, respectively. Since there is no information available to reliably identify the rupture geometry of the Edremit-Van event between the two Harvard CMT conjugate planes, we computed the CFF variation on both planes. The two planes are centered on the hypocentral location given by KOERI (43.234N, 38.430E), with dimensions 15×10 km², covering a depth range of about 0–10 km. In Fig. 5 we show the variation of CFF resulting on the two CMT planes. Both planes are loaded with positive CFF variations, with average values of 1.3 bar and 1.1 bar for the E-W and N-S planes, respectively. Peak

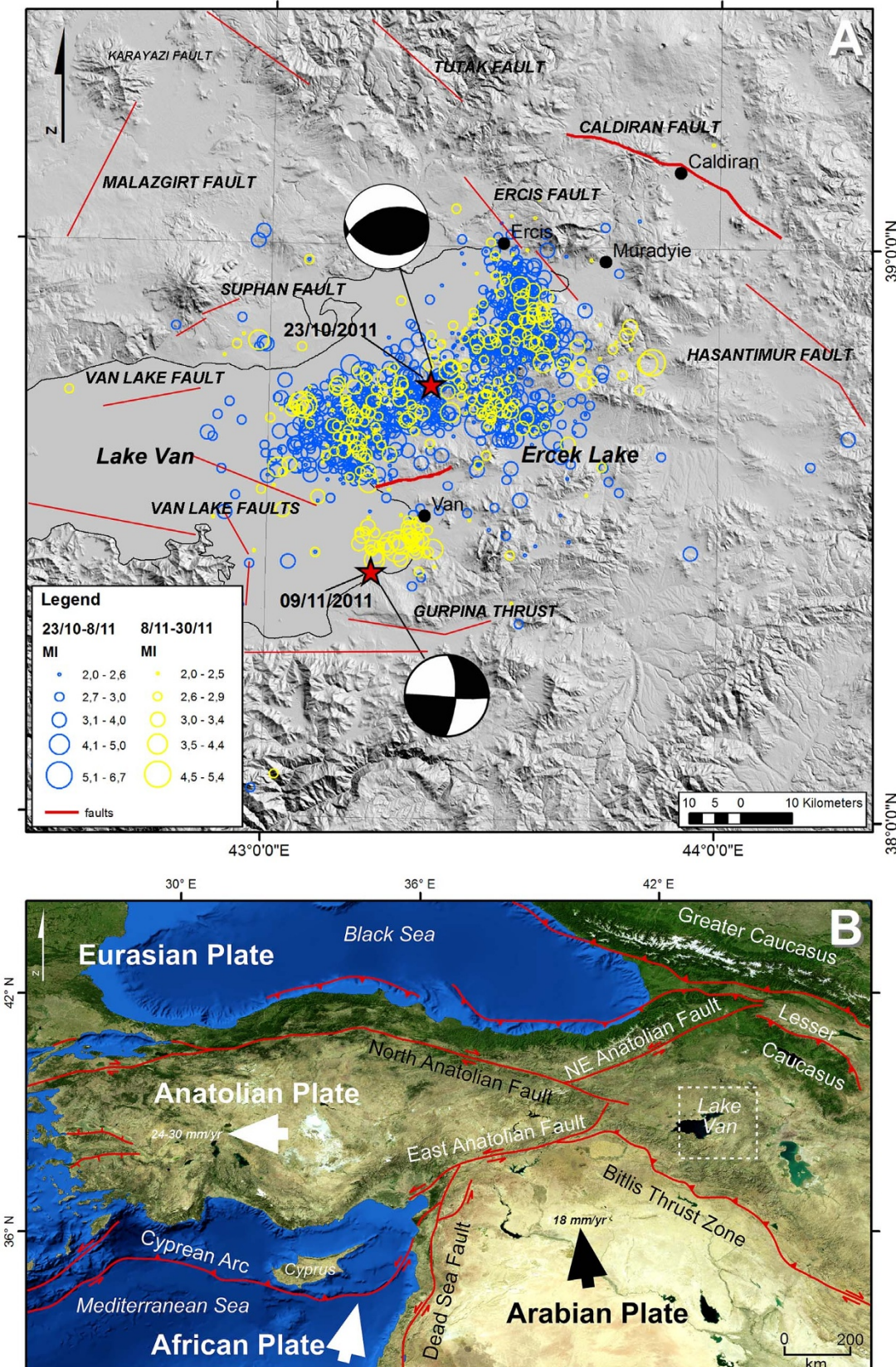


Figure 1 | (A) Aftershocks distribution following the October 23, 2011, mainshock: in blue up to November 9, 2011, earthquake; in yellow since November 9 and till November 30, 2011. Red lines represents the main active faults in the area, modified from SHARE “Seismic Hazard Harmonization in Europe” (www.share-eu.org). Figure 1A is not released under a Creative Commons Attribution-NonCommercial-ShareALike 3.0 Unported License. This image is licensed under a separate, Creative Commons Attribution-ShareAlike 3.0 Unported License. To view a copy of this licence visit <http://creativecommons.org/licenses/by-sa/3.0/> (B) Tectonic setting of the Eastern Mediterranean region. White and black arrows indicate the plate motion versus. Maps created with ARCGIS 10 software.

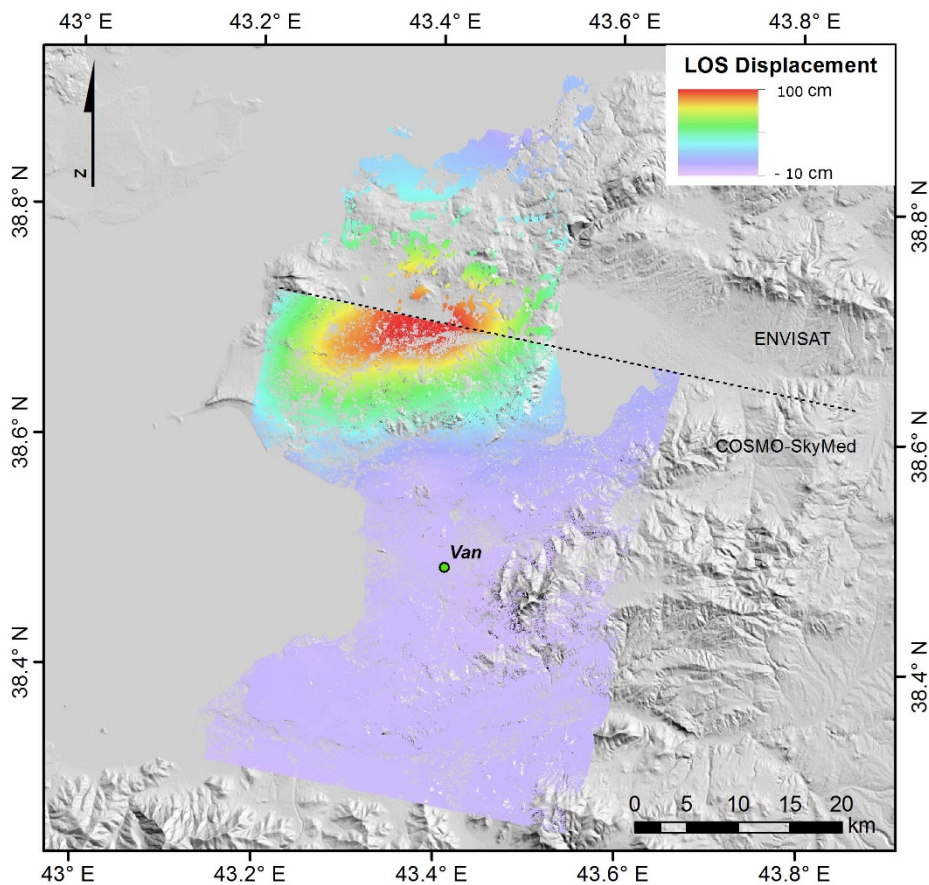


Figure 2 | Mosaic of unwrapped differential interferograms relative to the October 23, 2011 earthquake, from COSMO-SkyMed and ENVISAT coseismic pairs (south and north of the dashed line respectively). The ENVISAT dataset has been scaled to compensate the small discontinuity with respect to COSMO-SkyMed data mainly due to a different reference point selected for the unwrapping procedure, and the different LOS of the two satellites. The displacement is in LOS geometry. Maps created with ARCGIS 10 software.

CFF values (2.6 bar for the E-W plane and 3.0 bar for the N-S plane) are found on the deep portion for both planes.

Discussion

We have investigated the Van earthquake (October 23, 2011) by applying DInSAR technique and exploiting the capabilities of the

VHR SAR data acquired by COSMO-SkyMed and the C-band ENVISAT images. The COSMO-SkyMed differential interferogram has allowed to retrieve the surface displacement field. Since the DInSAR data does not cover the region located to the north of the event, we integrated SAR measurements with coseismic GPS offsets from the Turkish geodetic network.

The inference of the October 23 seismic source on the basis of geodetic data has been the subject of a set of studies^{36,37}. Fielding et al.³⁷ modeled the rupture as a single fault plane using SAR, GPS and seismic waveform data. On the other hand, Elliott et al.³⁶ modeled surface displacements from COSMO-SkyMed and ENVISAT with a pair en-echelon fault planes. Both studies indicate a deep rupture, with significant slip at 8 km depth, a dip range between 40 and 54 degrees. In our analysis, we modeled the fault with a single plane. Our most probable solution has a mixed thrust-left slip on a plane dipping NNW at about 50 degrees, consistently with the cited results even if slightly larger than the dip from Harvard CMT. Moreover the strike is consistent with seismological and geodetic estimate. Most of the slip occurs on a patch of about $15 \times 10 \text{ km}^2$, approximately located at depths between 10 and 18 km. The location and extents of the high slip patch is consistent with the peak slip area obtained by Fielding et al.³⁷. Probability density functions for model parameters (Fig. S2) shows that the position, geometry and along-strike extents of the fault plane are well resolved, while trade-offs exist among depth, slip and along-dip extents, which is a well-known limitation of geodetic source inversions³⁹. The highest residuals (Fig. 4a) are in the central part of the northern edge of the COSMO-SkyMed frame, where boundary effects maybe present, and along the eastern portion of the fault surface trace, supporting

Table 1 | Fault parameters for the October 23, 2011 earthquake resulting from the joint inversion of the DInSAR (COSMO-SkyMed and ENVISAT) and GPS dataset

	Most probable model	95% confidence interval
UTM X (km)	357.7	-4.0 +4.0
UTM Y (km)	4640.9	-4.0 +3.0
Top depth (km)	9.8	-2.7 +3.3
Strike	252.0	-7.0 +6.0
Dip	50.3	-5.5 +4.5
Rake	74.4	-8.8 +8.0
Slip (m)	3.8	-1.2 +3.4
Fault length (km)	20.7	-7.0 +7.7
Fault width (km)	16.9	-9.3 +9.8

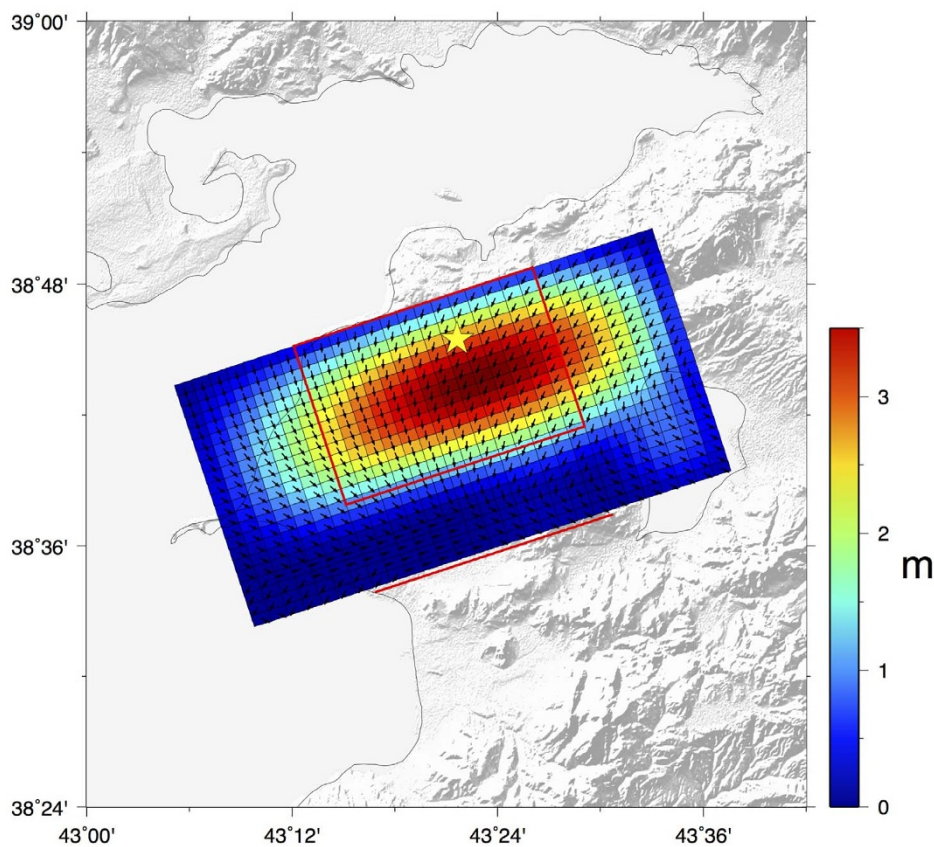


Figure 3 | Slip distribution model for the October 23, 2011 event A yellow star mark the epicentral location provided by KOERI. A red box mark the position and extents of the fault plane obtained in the nonlinear inversion step. Maps created with GMT software.

the hypothesis of a discontinuity in the strike direction as suggested by Elliot et al.³⁶. GPS horizontal offsets (Fig. 4b) are well recovered by the model, while the largest offsets (at sites MURA and OZAL) in the vertical component are overestimated, even though residuals are well within a standard deviation.

Finally, we investigated the effect of the perturbation to regional stress field induced by the mainshock on the November 9 earthquake through the evaluation of the CFF variation. For the Edremit-Van earthquake, Harvard CMT solution provides a N-S and an E-W conjugate planes, both with strike-slip geometries. The E-W plane is the most convincing; this conclusion is supported by field evidences found by Selcuk et al.³⁴. However, since it is not possible at present to reliably solve the ambiguity between the two geometries, the CFF variation has been computed on the two conjugate planes (Fig. 5). We found that both are loaded with stress levels up to 2.5–3.0 bar, largely exceeding the threshold value of 0.1 bar that is widely used to assess effective triggering of seismic events^{3,10}. These findings, in agreement with previous results by Akinci & Antonioli³³, support the hypothesis that the Edremit-Van earthquake has been actively promoted by the October 23 Van event.

Methods

In order to study the surface effect of the two main events, we have applied DInSAR method to a dataset composed of four pairs of images. The first, one was acquired by the Italian COSMO-SkyMed satellite, the second one by the European ENVISAT platform, and the two other pairs by the German TerraSAR-X. COSMO-SkyMed and TerraSAR-X satellites are equipped with an active X-band microwave sensor, while ENVISAT SAR is a C-band system, all capable to achieve cloud-free and day-and-night land observations. The X-band images are acquired in Stripmap mode at 3 m spatial resolution, and the ENVISAT data are in IS6 mode (<https://earth.esa.int/handbooks/asar/>), at about 20 m spatial resolution. The COSMO-SkyMed and ENVISAT data, both along ascending orbit, have been used to investigate the October 23 mainshock. In particular, the post-event image of COSMO-SkyMed is dated October 23, only few hours after the seismic event, while pre-seismic one was acquired

on October 10, 2011. The ENVISAT scenes were taken on July 22, 2011, and November 19, 2011. It is worth to note that the time interval between these two images includes also the strong aftershock occurred on November 9. We selected from ENVISAT interferogram the portion that complete to the north the surface displacement measured from COSMO-SkyMed dataset (see Fig. 2), and which was not affected by the November aftershock, as confirmed by TerraSAR-X interferograms.

TerraSAR-X images have been used to measure the deformation caused by the November 9, 2011, earthquake. In this case for the descending pair, the pre-seismic image is acquired few hours before the earthquake, while the post-seismic one is dated November 20, 2011. Concerning the ascending pair, the pre-seismic image is ten days before the earthquake (31/10/2011), the post-seismic image two days after (11/11/2011).

In order to improve the signal-to-noise ratio, a 2 by 2 multi-look factor in slant-range and azimuth has been applied to the COSMO-SkyMed and TerraSAR-X interferograms, with a square pixel of about 6 m. The 90 m Shuttle Radar Topography Mission (SRTM) digital elevation model has been used to remove the topographic contribution of the interferometric phase. Since the temporal baseline is sufficiently short, both interferograms maintain a good coherence, allowing capturing most of the coseismic deformation. Before the retrieval of the Line Of Sight (LOS) displacements using a minimum cost flow phase unwrapping algorithm, the phase noise has been reduced applying an adaptive filter⁴⁰.

Concerning the lower resolution data coming from ENVISAT, we computed the interferogram by using a multi-look factor equal to 1×5 , in range and azimuth respectively, and by applying the same phase noise reduction and unwrapping methods of X-band data. DORIS precise orbital data have been used to correct possible orbital fringes. Despite the low interferometric coherence of ENVISAT interferogram, caused by the long time interval (temporal baseline), the unwrapped data have contributed to improve the spatial coverage and to better constrain the model retrieval.

We jointly inverted DInSAR (COSMO-SkyMed and ENVISAT) and GPS data using a two-step method: we first inferred the geometric features of the Van earthquake source with a non-linear inversion assuming a uniform slip, then we retrieved the slip distribution on the fault plane with a linear inversion. For the inversion procedure, a combined DInSAR deformation field has been obtained by selecting the ENVISAT field laying in the region not covered by COSMO-SkyMed data and merging this subfield with the full COSMO-SkyMed field. In regions where both datasets are available, we used only the COSMO-SkyMed dataset that, because of its shorter temporal baseline, it is less affected by post-seismic effects. The resulting combined dataset has been downsampled by a factor of 0.5 for computational reasons.

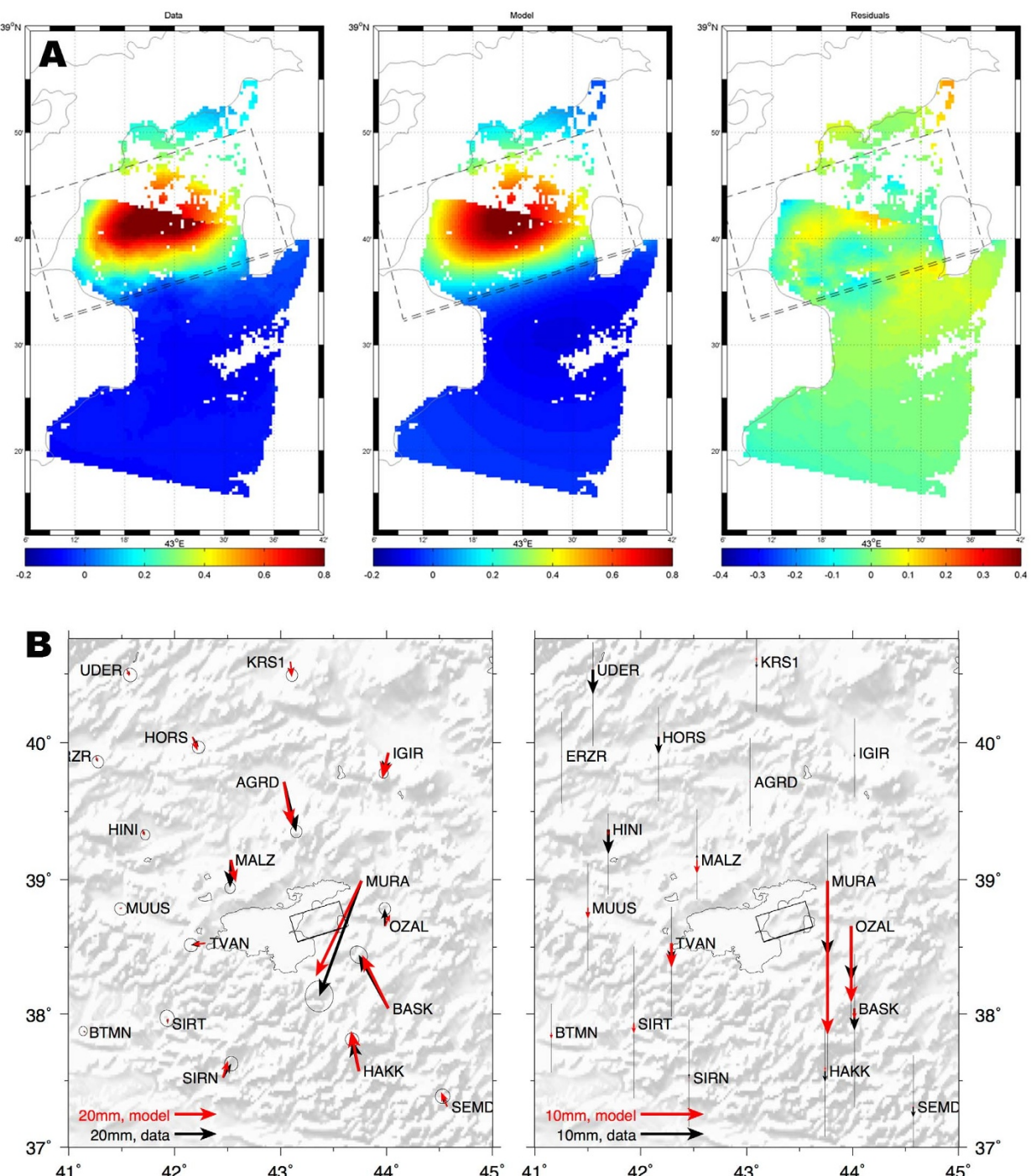


Figure 4 | (A) Observed (left) and modeled (center) DInSAR deformation fields. Residuals (right) are defined as the difference between observed and modeled displacements. The surface projection of the source model is also shown as a dashed box. The vertical shift between the COSMO-SkyMed and ENVISAT displacement is due to the different absolute references for the two datasets. (B) Observed and modeled horizontal (left panel) and vertical (right panel) GPS deformation fields. Error ellipses in the left panel and vertical bars in the right panel correspond to 68% confidence levels. The GPS offsets show a compressional deformation regime, consistently with the expected thrust mechanism; the largest offset of about 6 cm is found at the near-field site MURA. Maps created with the GMT software.

For the nonlinear inversion procedure we modeled the deformation field for a given fault plane using the analytical expressions from Okada⁴¹, assuming an homogeneous Poisson half-space. To take into account the different characteristics of DInSAR and GPS datasets, we applied different weights to each in order to obtain similar contributions to the total misfit for models that give an equivalent fit to the data. We used a Bayesian inference scheme to estimate the probability distribution functions (PDF) of fault parameters through a Markov-chain Monte Carlo integration³⁵. Since the COSMO-SkyMed and ENVISAT datasets have different absolute references, we included in the model parameters a “bias” value between the two datasets.

Once the geometry is fixed, we estimated the slip distribution on the fault plane with a linear inversion. We extended the fault plane resulting from the uniform inversion up to $40 \times 30 \text{ km}^2$ in order to better account for (eventual) slip heterogeneities, and subdivided it into patches of size of about $1.5 \times 1.5 \text{ km}^2$. We composed a Green Function matrix by imposing a unitary slip on each patch and computing the corresponding deformation fields for DInSAR and GPS data, according to the Okada analytical expressions⁴¹. The slip distribution is then recovered by simultaneously minimizing (in the least-squares sense) the total chi-squared and a discrete approximation of the Laplacian to avoid large, unphysical oscillations in slip values. The solution is computed assuming a positivity constraint on the model, with an

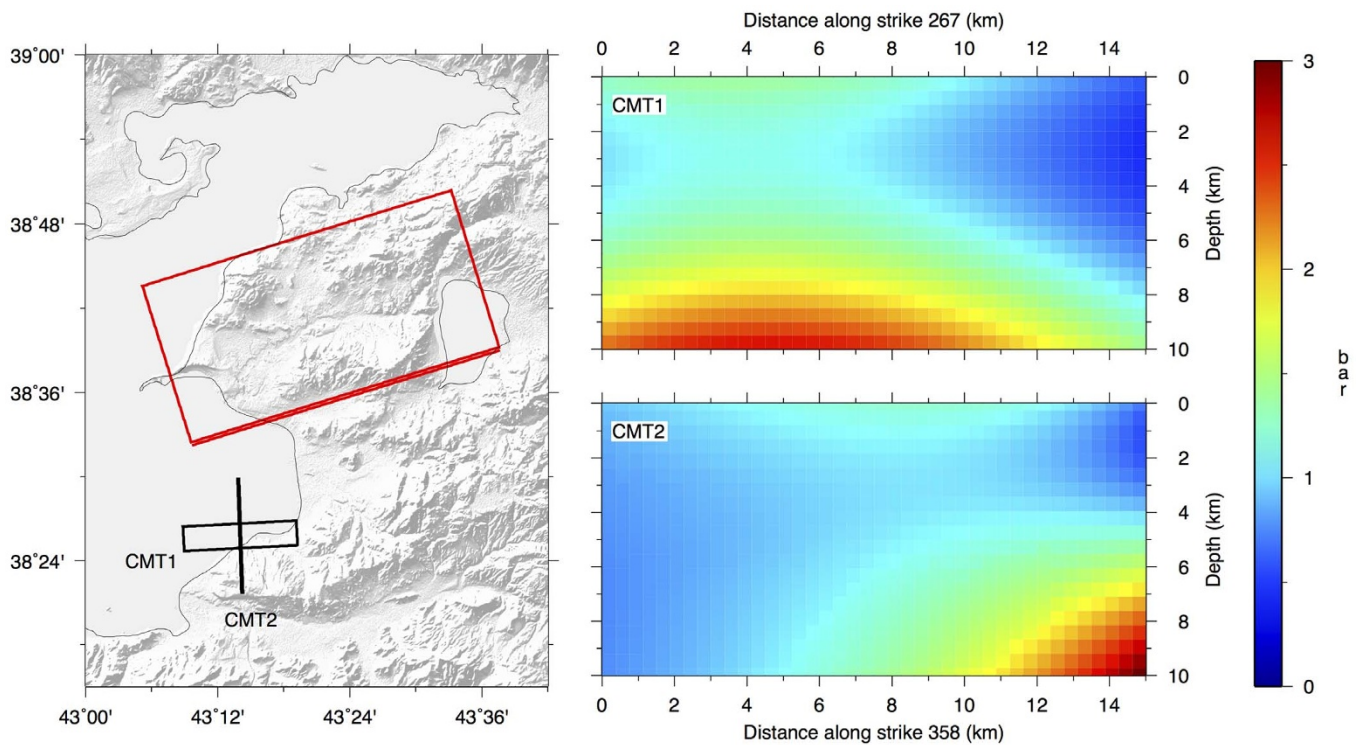


Figure 5 | CFF variations induced by the October 23, 2011 event on the November 9, 2011 rupture plane for both Harvard CMT solutions. In the left panel, a red box marks the position of the modeled fault plane for the mainshock, while black boxes mark the positions of both CMT nodal planes. Maps created with the GMT software.

optimized version of the Lawson-Hanson method^{42,43}. The inclusion of a smoothing term to damp unphysical model oscillations introduces a tradeoff between data fit and solution roughness. We determined the weight of the smoothing constraint by evaluating a misfit-roughness tradeoff curve (figure S3).

We estimated the spatial resolution for the slip distribution on fault plane by defining a checkerboard synthetic slip model. The resulting slip distributions have been computed with the coverage of SAR and GPS data and inverted with the same procedure used for the real datasets. Results (Figure S4) show that a resolution of about 5 km can be expected up to ~5 km depth, while at greater depths model resolution decreases to over 10 km.

We then investigated the role of the Van earthquake in promoting the rupture of the Van-Edremit earthquake by evaluating the Coulomb Failure Function (CFF). Using the source model obtained for the Van earthquake, the elastic strain tensor corresponding to the seismic dislocation is computed with the analytical solutions provided by Okada⁴¹. Using standard relations from elasticity theory, the strain field is converted into an incremental stress tensor that acts as a perturbation of the pre-existing (unknown) regional stress field. The effect of the perturbation to the stress field on a given fault mechanism is then assessed by computing the CFF variation, defined as $\Delta\text{CFF} = \Delta\tau + \mu(\Delta\sigma_n + \Delta p)$, where $\Delta\tau$ and $\Delta\sigma_n$ are respectively the shear and normal incremental stresses, μ is the friction coefficient and Δp is the pore pressure change⁴⁴. It is convenient to rewrite this relation as $\Delta\text{CFF} = \Delta\tau + \mu_e\Delta\sigma_n$, where μ_e is an effective friction coefficient taking into account static friction, hydrostatic pressure and pore fluid pressure^{3,7}. We assumed $\mu_e = 0.4$, a value consistent with laboratory evidences on friction and moderate pore pressure in conditions where fluids are not fully expelled⁴⁵. Knowing the values of ΔCFF on a given fault mechanism allows to establish whether the stress field is acting to promote ($\Delta\text{CFF} > 0$) or oppose ($\Delta\text{CFF} < 0$) the rupture. As a general rule, a CFF increase of 0.1 bar (corresponding to tidal load) is considered in literature as effective for earthquake triggering¹⁰.

- Stein, R. S. The role of stress transfer in earthquake occurrence. *Nature* **402**, 605–609 (1999).
- Harris, R. A. Introduction to special section: stress triggers, stress shadows, and implications for seismic hazard. *J. Geophys. Res.* **103**, 24347–24358 (1998).
- Stein, R. S., King, G. C. P. & Lin, J. Change in failure stress on the southern San Andreas fault system caused by the 1992 magnitude = 7.4 Landers earthquake. *Science* **258**, 1328–1332 (1992).
- Harris, R. A. & Simpson, R. W. Changes in static stress on southern California faults after the 1992 Landers earthquake. *Nature* **360**, 251–254 (1992).
- Jaumé, S. C. & Sykes, L. R. Change in the state of stress on the southern San Andreas fault resulting from the California earthquake sequence of April to June 1992. *Science* **258**, 1325–1328 (1992).

- Stramondo, S. et al. Did the September 2010 (Darfield) earthquake trigger the February 2011 (Christchurch) event? *Sci. Rep.* **1**, 98, (2011) doi:10.1038/srep00098
- King, G. C. P. & Cocco, M. Fault interaction by elastic stress changes: New clues from earthquake sequences. *Adv. Geophys.* **44**, 1–38 (2001).
- Freed, A. M. Earthquake triggering by static, dynamic and postseismic stress transfer. *An. Rev. Earth Planet. Sci.* **33**, 335–367 (2005).
- Steacy, S., Gomberg, J. & Cocco, M. Introduction to special section: Stress transfer, earthquake triggering, and time-dependent seismic hazard. *J. Geophys. Res.* **110**, B05S01 (2005).
- King, G. C. P., Stein, R. S. & Lin, J. Static stress changes and the triggering of earthquakes. *Bull. Seismol. Soc. Am.* **84**, 935–953 (1994).
- Melini, D., Casarotti, E., Piersanti, A. & Boschi, E. New insights on long distance fault interaction. *Earth Planet. Sci. Lett.* **204**, 363–372 (2002).
- Toda, S. & Stein, R. S. Toggling of seismicity by the 1997 Kagoshima earthquake couplet: A demonstration of time-dependent stress transfer. *J. Geophys. Res.* **108**, 2567 (2003).
- Dieterich, J. H. Earthquake nucleation on faults with rate and state-dependent friction. *Tectonophysics* **211**, 115–134 (1992).
- Gomberg, J., Reasenberg, P., Cocco, M. & Belardinelli, M. E. A frictional population of seismicity rate change. *J. Geophys. Res.* **110**, B05S03 (2005).
- Toda, S., Stein, R. S., Reasenberg, P., Dieterich, J. H. & Yoshida, A. Stress transferred by the 1995 Mw = 6.9 Kobe, Japan, shock: Effect on aftershocks and future earthquake probabilities. *J. Geophys. Res.* **103**, 24543 (1998).
- Toda, S., Stein, R. S., Richards-Dinger, K. & Bozkurt, S. B. Forecasting the evolution of seismicity in southern California: Animations built on earthquake stress transfer. *J. Geophys. Res.* **110**, B05S16 (2005).
- Dieterich, J. H., Cayol, V. & Okubo, P. The use of earthquake rate changes as a stress meter at Kilauea volcano. *Nature* **408**, 457–460 (2000).
- Llenos, A. L., McGuire, J. J. & Ogata, Y. Modeling seismic swarms triggered by aseismic transients. *Earth Planet. Sci. Lett.* **281**, 59–69 (2009).
- Kandilli Observatory And Earthquake Research Institute (2011) 23 October 2011, Mw = 7.2 Van, Turkey Eq. Available at: http://www.koeri.boun.edu.tr/News/23_October_2011, Mw=7.2 Van, Turkey Eq._16_204.depmuh (Accessed: 21/10/2013).
- Kein, İ. Van Gölü ile Iran Sınırı arasındaki bölgede yapılan Jeoloji Gözlemlerinin Sonuçları Hakkında Kısa Bir Açıklama. *Butteten of the Geological Bodety of Turkey* **20**, 79–85 (1977).
- U.S. Geological Survey, National Earthquake Information Center (2011) Magnitude 7.1 - EASTERN TURKEY. Available at: <http://earthquake.usgs.gov/earthquakes/eqinthenews/2011/usb0006bqc/> (Accessed: 21/10/2013).
- GFZ moment tensor solution (2011) 23 October 2011, Mw = 7.2 Van, Turkey Eq. Available at: <http://geofon.gfz-potsdam.de/data/alerts/2011/gfz2011utuo/mt.txt> (Accessed: 21/10/2013).



23. Kandilli Observatory And Earthquake Research Institute (2011) *09 November 2011, M = 5.6, Van, Turkey Eq.* Available at: http://www.koeri.boun.edu.tr/News/09%20November%202011,%20M=5.6,%20Van,%20Turkey%20Eq._16_206.depmuh (Accessed: 21/10/2013).
24. Bayrak, Y. *et al.* Estimating earthquake hazard parameters from instrumental data for different regions in and around Turkey. *Eng. Geol.* **105**, 200–210 (2009).
25. McKenzie, D. P. Active tectonics of the Mediterranean region. *Geophys. J. R. Astron. Soc.* **30**, 109–185 (1972).
26. McClusky, S. *et al.* Global positioning system constraints on plate kinematics and dynamics in the eastern Mediterranean and Caucasus. *J. Geophys. Res.* **105**, 5695–5719 (2000).
27. Özkaraymak, Ç., Yürür, T. & Köse, O. An example of intercontinental active collisional tectonics in the Eastern Mediterranean region (Van, Eastern Turkey). Paper presented at The Fifth Int. Symp. On Eastern Mediterranean Geology, Thessaloniki. T1–44(2004).
28. Berberian, M. [Seismic sources of the Transcaucasian historical earthquakes] *Historical and Prehistorical Earthquakes in the Caucasus* [Giardini, D., Balassanian, S. (ed.)] [233–311] (NATO ASI Series, 2. Environment, 28Kluwer Academic, The Netherlands, 1997).
29. Tchalenko, J. S. A reconnaissance of the seismicity and tectonics at the northern border of the Arabian plate (Lake Van region). *Rev. Géogr. phys. Geol. dyn.* **19**, 189–208 (1977).
30. Toksoz, M. N., Arpat, E. & Saroglu, F. East Anatolian earthquake of 24 November 1976. *Nature* **270**, 423–425 (1977).
31. Covello, F. *et al.* COSMO-SkyMed an existing opportunity for observing the Earth. *Journal of Geodynamics* **49**, 171–180 (2010).
32. Pitz, W., & Miller, D. The TerraSAR-X Satellite. *IEEE Trans. on Geosc. and Rem. Sens.* **48**, 615–622 (2010).
33. Akinci, A. & Antonioli, A. Observations and stochastic modelling of strong ground motions for the 2011 October 23 Mw 7.1 Van, Turkey, earthquake. *Geophys. J. Int.* **192**, 1217–1239 (2013).
34. Selcuk, L., Selcuk, A. S. & Beyaz, T. Probabilistic seismic hazard assessment for lake Van basin, Turkey. *Nat. Hazards* **265**–271 (2010).
35. Sambridge, M. Geophysical inversion with a neighbourhood algorithm - II. Appraising the ensemble. *Geophysical J. Int.* **128**, 727–746 (1999).
36. Elliott, J. R., Copley, A. C., Holley, R., Scherer, K. & Parsons, B. The 2011 Mw 7.1 Van (Eastern Turkey) earthquake. *J. Geophys. Res.* **118**, 1619–1637 (2013).
37. Fielding, E. J., Lundgren, P. R., Taymaz, T., Yolsal-Cevikbilen, S. & Owen, S. E. Fault-slip source models for the 2011 Mw 7.1 Van Earthquake in Turkey from SAR Interferometry, Pixel Offset Tracking, GPS, and Seismic Waveform Analysis. *Seismol. Res. Lett.* **84**, 579–593 (2013).
38. Doğan, B. & Karakaş, A. Geometry of co-seismic surface ruptures and tectonic meaning of the 23 October 2011 Mw 7.1 Van earthquake (East Anatolian Region, Turkey). *Journal of Structural Geology* **46**, 99–114 (2012).
39. Hernandez, B., Cotton, F. & Campillo, M. Contribution of radar interferometry to a two-step inversion of the kinematic process of the 1992 Landers earthquake. *J. Geophys. Res.* **104**, 13083–13099 (1999).
40. Goldstein, R.-M. & Werner, C. L. Radar interferogram filtering for geophysical applications. *Geoph. Res. Letters* **25**, 4035–4038 (1998).
41. Okada, Y. Surface deformation due to shear and tensile faults in a half-space. *Bull. Seismol. Soc. Am.* **82**, 1018–1040 (1992).
42. Lawson, C. L. & Hanson, R. J. *Solving least squares problems*. (Prentice-Hall, Englewood Cliffs, NJ, 1974).
43. Van Benthem, M. H. & Keenan, M. R. Fast algorithm for the solution of large-scale non-negativity-constrained least squares problems. *J. Chemometrics* **18**, 441–450 (2004).
44. Reasenberg, P. A. & Simpson, R. W. Response of Regional Seismicity to the static stress change produced by the Loma Prieta Earthquake. *Science* **7**, 1687–1690 (1992).
45. Stein, R. S., Barka, A. & Dieterich, J. Progressive failure on the North Anatolian fault since 1939 by earthquake stress triggering. *Geophys. J. Int.* **128**, 594–604 (1997).

Acknowledgments

We would thank Dr. Can Zulfikar from KOERI (Istanbul) for his contribution to find scientific documents and reports concerning the Van earthquake. We also thank Dr. Semih Ergintav for providing GPS data. Marco Chini's contribution was supported by the National Research Fund of Luxembourg through the PAPARAZZI project (CORE C11/SR/1277979).

Author contributions

M.M. contributed to the analysis of seismotectonic regime of the region and the analysis of the results. M.C. and C.B. contributed to the DInSAR processing. V.C. and D.M. have provided the cff and source models. S.S. contributed to the analysis of the results and the discussion. M.S., M.P., C.K. and C.A.B. contributed to the discussion of the results. All authors contributed to write the manuscript.

Additional information

Supplementary information accompanies this paper at <http://www.nature.com/scientificreports/>

Competing financial interests: The authors declare no competing financial interests.

How to cite this article: M.M. *et al.* The October 23, 2011, Van (Turkey) earthquake and its relationship with neighbouring structures. *Sci. Rep.* **4**, 3959; DOI:10.1038/srep03959 (2014).

This work is licensed under a Creative Commons Attribution-NonCommercial-ShareAlike 3.0 Unported License. The images or other third party material in this article are included in the article's Creative Commons License, unless indicated otherwise in the credit line; if the material is not included under a Creative Commons license, users will need to obtain permission from the license holder to reproduce the material. To view a copy of this license, visit <http://creativecommons.org/licenses/by-nc-sa/3.0/>